

Depth-of-interaction measurement in a single-layer crystal array with a single-ended readout using digital silicon photomultiplier

This content has been downloaded from IOPscience. Please scroll down to see the full text.

2015 Phys. Med. Biol. 60 6495

(<http://iopscience.iop.org/0031-9155/60/16/6495>)

View [the table of contents for this issue](#), or go to the [journal homepage](#) for more

Download details:

IP Address: 147.47.228.219

This content was downloaded on 20/11/2015 at 00:17

Please note that [terms and conditions apply](#).

Depth-of-interaction measurement in a single-layer crystal array with a single-ended readout using digital silicon photomultiplier

Min Sun Lee^{1,2} and Jae Sung Lee^{1,2,3}

¹ Department of Nuclear Medicine, Seoul National University, Seoul 110–744, Korea

² Interdisciplinary Programs in Radiation Applied Life Science, Seoul National University, Seoul 110–744, Korea

³ Department of Biomedical Sciences, Seoul National University, Seoul 110–744, Korea

E-mail: jaes@snu.ac.kr

Received 18 November 2014, revised 22 June 2015

Accepted for publication 13 July 2015

Published 6 August 2015



CrossMark

Abstract

We present the first experimental evaluation of a depth-of-interaction (DOI) positron emission tomography (PET) detector using a digital silicon photomultiplier (dSiPM). To measure DOI information from a mono-layer array of scintillation crystals with a single-ended readout, our group has previously proposed and developed a new method based on light spread using triangular reflectors. Since this method relies on measurement of the light distribution, dSiPM, which has a fully digital interface, has several merits for our DOI measurement. The DOI PET detector comprised of a dSiPM sensor (DPC-3200-22-44) coupled with a 14×14 array of $2 \text{ mm} \times 2 \text{ mm} \times 20 \text{ mm}$ unpolished LGSO crystals. All crystals were covered with triangular reflectors. To obtain a good performance of the DOI PET detector, several parameters of detector were selected as a preliminary experiment. Detector performance was evaluated with the selected parameters and the optimal experimental setup, and a DOI measurement was conducted by irradiating the crystal block at five DOI positions spaced at intervals of 4 mm. Maximum-likelihood estimation was employed for DOI positioning and the optimal DOI estimation scheme was also investigated in this study. As a result, the DOI PET detector showed clear crystal identification. The energy resolution (full-width at half-maximum (FWHM)) averaged over all depths was $10.21\% \pm 0.15\%$ at 511 keV, and time resolution averaged over all depths was 1198.61 ± 39.70 ps FWHM. The average DOI positioning accuracy for all depths was $74.22\% \pm 6.77\%$, which equates to DOI resolution of 4.67 mm. Energy and DOI resolutions

were uniform over all crystal positions except for the back parts of the array. Furthermore, additional simulation studies were conducted to verify the results of our DOI measurement method that is combined with dSiPM technology. In conclusion, our continuous DOI PET detector coupled with dSiPM is a promising PET/MRI detector with DOI-encoding capability.

Keyword: PET, depth of interaction, scintillation detector, silicon photomultiplier, digital silicon photomultiplier

(Some figures may appear in colour only in the online journal)

1. Introduction

Positron emission tomography (PET) is a functional and molecular imaging tool that has greatly contributed to the biomedical research and clinical practice (Im *et al* 2013, Kim *et al* 2013, Lee and Park 2014). Recently, PET detectors with high resolution and high sensitivity have received great interest especially for pre-clinical and organ-specific imaging (Cherry *et al* 1997, Yamaya *et al* 2008, Yamamoto *et al* 2011). PET scanners with a small field of view (FOV) and relatively long crystal elements lose resolution in the peripheral region of the field of view owing to mispositioning of the line of response, which is known as the parallax error. The main way to reduce parallax error is to use the depth-of-interaction (DOI) encoding capability of detectors. Using DOI information in detectors, the parallax error can be reduced and a PET system can thus achieve fine resolution and high sensitivity simultaneously (Moses and Derenzo 1994, MacDonald and Dahlbom 1998, Yang *et al* 2008). Enhanced resolution in the peripheral FOV offers uniform spatial resolution and image contrast. In addition, the high sensitivity of a PET system increases the signal-to-noise ratio, thus reducing the radiation dose and scan time. Therefore, knowing the exact DOI information of a gamma-ray detector is regarded as crucial in high-resolution small-ring PET systems.

Various DOI measurement methods have been proposed, including discrete DOI measurements using multiple layers of crystals and/or photosensors and continuous DOI measurements using double-sided readouts, light sharing within a crystal array, and statistical methods using monolithic crystals (Miyaoaka *et al* 1998, Joung *et al* 2002, Yang *et al* 2006, Ito *et al* 2010a, 2010b). However, many of these approaches have high manufacturing costs because of the large number of crystal elements, photosensors, and/or readout channels to deal in the electronics (Ito *et al* 2011). Hence, several groups including our own have concentrated on the development of novel DOI measurement methods that have reduced manufacturing cost and complexity while maintaining the DOI-encoding accuracy (Du *et al* 2009, Miyaoaka *et al* 2009, Ito *et al* 2010a, 2013, van Dam *et al* 2011).

We previously proposed a novel DOI measurement method employing a single-layer array of scintillation crystals and a single-ended readout based on light spreading within the crystal array (Ito *et al* 2010a). The scintillation crystal array is wrapped with reflectors having triangular teeth, such that scintillation photons spread simply in the x -direction in the upper halves of the crystal and in the y -direction in the lower halves. Accordingly, DOI positions are estimated by considering the extent and direction of the dispersion of light in 2D. The DOI detector design is detailed in section 2.1.1. We previously developed a prototype DOI PET detector module composed of a single-layer pixelated LGSO crystal array and a single-ended multi-channel photomultiplier tube (PMT). The prototype continuous DOI PET detector showed promise in high-resolution and high-sensitivity applications (Ito *et al* 2013).

Silicon photomultiplier (SiPM) has received great attention as an alternative photosensor to the PMT owing to its insensitivity to magnetic fields, high gain, ruggedness, and fast timing properties (Schaart *et al* 2009, Kwon *et al* 2011, Yoon *et al* 2012, Kwon and Lee 2014). Recently, digital SiPM (dSiPM), a new class of light detector developed by Philips Digital Photon Counting, has received attention owing to its all-digital photon counting (digital-in/digital-out). The dSiPM is operated with single-photon avalanche photodiodes (SPADs) working as digital switches with their own readout circuits. Each SPAD with active quenching and recharging capability generates an output signal to yield a digital sum of photon counts on the pixel level. Moreover, integration of sensor parts and pixel-level readout circuits simplifies the electronics (Frach *et al* 2009).

Here, we combined our continuous DOI-encoding method with dSiPM technology and experimentally evaluated its performance since dSiPM has several merits in investigating and realizing our DOI PET detector and system. The most important advantage is that the individual readout of the energy and timing information from each pixel of dSiPM is simple compared with that of analog SiPMs or PMTs, which require additional complex readout and digitizing electronics. Simple and easily implemented individual readouts are crucial to our DOI measurement method, which relies on the estimation of the light distribution within the crystal block.

In this study, a 14×14 unpolished LGSO crystal ($2.0 \text{ mm} \times 2.0 \text{ mm} \times 20 \text{ mm}$) array covered with reflectors having triangular teeth was assembled with dSiPM. A preparatory study was conducted prior to the detector performance evaluation where the acquisition coincidence window, temperature, and several sensor configurations were selected leading to the optimal performance. Optimization of DOI estimation scheme was also held for the successful depth positioning. From the results of the aforementioned study, the detector performance was investigated with selected parameters under the optimal conditions. The DOI-encoding capability of the detector was investigated and DOI information was extracted employing maximum-likelihood estimation. Finally, further simulation studies were conducted to verify the merits of dSiPM on our DOI measurement design while taking account of dark count noise, electronic noise from readout circuits, and the complexity of the readout scheme.

2. Materials and methods

2.1. Materials

2.1.1. Continuous DOI-encoding detector. Previously, our group proposed a novel PET detector concept to measure continuous DOI information from a single-layer crystal array using a single-ended readout (Ito *et al* 2010a). The principle of the continuous DOI-encoding detector (referred to as the cDOI detector) is that the light spreading within the crystal array partially covered with reflectors having triangular teeth shape crossed over to each other (figure 1(a)). Because of the reflector configuration, different light dispersion patterns are attainable along the x - and y -directions depending on the gamma-ray interaction depth (figure 1(b)). Different 2D light dispersion patterns for different DOI positions are observed from the detector response function of photosensors. Consequently, DOI positions can be estimated by considering the statistical characteristics of the detector response function representing the light distribution. For an exact estimation of the DOI position, accurate measurement of the light distribution is crucial. Methods of DOI position estimation is detailed in section 2.2.2.4.

To construct the DOI-encoding detector, Philips dSiPM sensor (DPC-3200-22-44) was coupled with a single-layer pixelated scintillation crystal array as illustrated in figure 2(a). The crystal array consisted of 14×14 chemically unpolished LGSO crystals ($\text{Lu}_{1.9}\text{Gd}_{0.1}\text{SiO}_5 : \text{Ce}$;

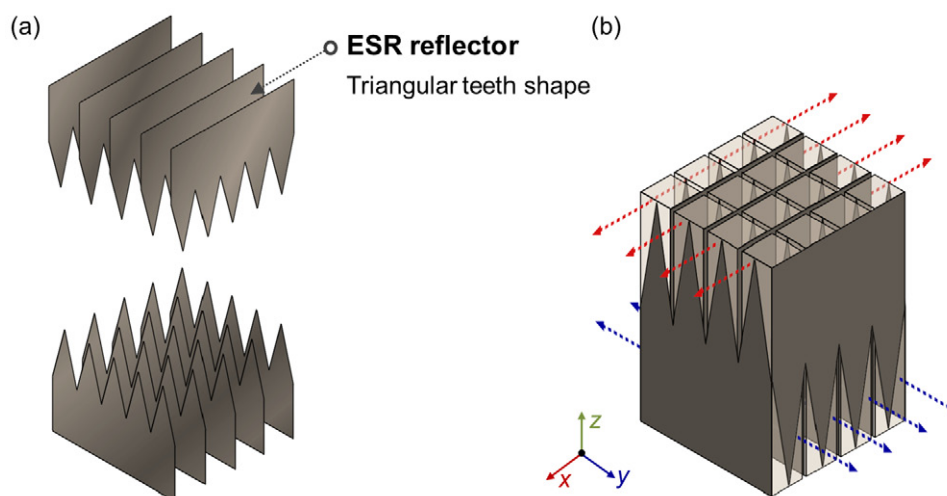


Figure 1. Concept of the continuous DOI-encoding detector. (a) Reflectors having triangular teeth cross each other, (b) and crystals are inserted in the reflector grid. Different 2D light dispersion patterns are observed depending on the gamma-ray interaction position within the crystal array. Hence, DOI information can be extracted from different light dispersion patterns recorded as different detector responses.

Hitachi Chemical, Tokyo, Japan) with a pixel size of $2.0\text{ mm} \times 2.0\text{ mm} \times 20\text{ mm}$. Each crystal was wrapped with a 3M enhanced specular reflector (ESR, 3M) grid constructed by crossing reflector strips with triangular teeth. A light guide with a thickness of 1 mm covering the active area of the sensor was inserted between the sensor and crystal array to efficiently spread light across the pixels. Additionally, a window-shaped reflector was inserted between the sensor and light guide to reduce the light loss in the 0.8 mm-wide dead spaces between pixels (figure 2(b)). All components were optically coupled using optical grease (BC-630, OKEN, Japan).

2.1.2. Digital silicon photomultiplier (dSiPM). The sensor consists of 4×4 independent dies, and each die is further divided into 2×2 pixels resulting in a total of 8×8 pixels per sensor. Each pixel is again sub-divided into 2×2 sub-pixels. A pixel has dimensions of $3.2\text{ mm} \times 3.8775\text{ mm}$, and each pixel consists of 3200 SPADs (figure 2(b)).

The data acquisition cycle of dSiPM works for individual dies, and it starts with a trigger signal generated when the number of detected photons exceeds the trigger threshold controlled by the trigger network. The configurable trigger network works at the pixel level, providing four different photon count thresholds based on the Boolean logic of four sub-pixels; each are indicated as trigger schemes 1, 2, 3, and 4. Trigger scheme 1 refers to the generation of a trigger signal with one photon count among any of the four sub-pixels, while trigger scheme 4 refers to the generation of a trigger signal when all four sub-pixels detect at least one photon count. The trigger signal is then validated using another configured threshold, which takes a certain length of time (40 ns validation interval was used in this study). The validation network works at the sub-pixel level, in a manner similar to the trigger network. SPADs in a sub-pixel are grouped into eight sections (row-trigger-lines), and the eight sections are paired into four different two-input logic gates. The configuration of logic gates is set by different validation schemes (validation schemes 1, 2, 4, and 8). A higher validation scheme has a higher photon count threshold at the sub-pixel level. If the validation threshold is exceeded, photons are collected during the integration period (165 ns integration time used in this study) and the number of fired cells in each pixel

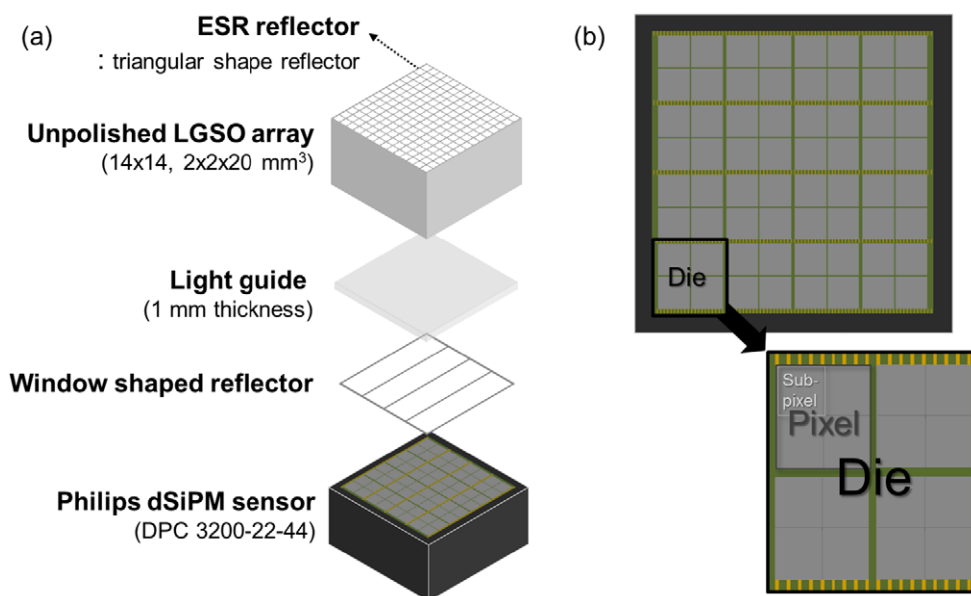


Figure 2. (a) Components of the cDOI-dSiPM detector. (b) Basic structure of dSiPM. dSiPM is composed of 4×4 dies, and each die is sub-divided into four pixels. Pixels are further sub-divided into four sub-pixels.

is summed and sent to the readout buffer which takes another 680 ns. In this step, each die gives four photon count values per event. After readout, entire cells are globally recharged for 20 ns and dies are ready for the new acquisition cycle. If the event is not validated, the pixel is immediately recharged (Frach *et al* 2009, PDPC-TEK User Manual 2014).

However, since each die independently proceeds in its own acquisition cycle, only dies that fulfill trigger and validation thresholds record their photon counts. Accordingly, dies in low-intensity regions cannot start their own acquisition sequence, and photon counting information is thus missed in the peripheral region of the light distribution. To resolve this problem, dSiPM has a neighbor logic (NL) configuration that forces an event acquisition cycle on neighboring dies that do not satisfy trigger and validation thresholds. As long as the master die detects an event while exceeding trigger and validation thresholds, it sends the SYNC signal to neighboring slave dies. This SYNC signal bypasses the trigger and validation networks in slave dies, and photons are thus detectable in the outer event regions. NL is operated in two different configurations, normal NL and full-tile NL. Normal NL forcefully triggers dies in the vertically and horizontally adjacent groups, while full-tile NL forcefully triggers all other dies in the sensor. In this study, we applied full-tile NL to acquire full-tile information because the light distribution information across all dies provides the flexibility in DOI estimation scheme.

Data were acquired using a Technical Evaluation Kit for dSiPM (Philips Digital Photon Counting), which sends the acquired data to a personal computer via a USB connection.

2.2. Measurement and performance evaluation

2.2.1. Parameter selection of the detector system

2.2.1.1. Experimental conditions and setup. For the successful implementation of cDOI measurement using dSiPM, various sensor configurations and system settings were tested to find the best suited settings. Parameters were determined to obtain sufficiently high full-tile

triggering ratio, high effective event ratio, good energy resolution, and clear crystal identification. Several parameters were considered: the acquisition coincidence time window, the temperature of the experimental setting, and the trigger and validation scheme. Details of each parameter control will be described in the next section.

A full-tile NL configuration was used for each experimental setup to acquire pixel values from all 4×4 dies and thus examine the light distribution of the cDOI detector. The validation length was set to 40 ns, and the integration length was set to 165 ns. The 10% of cells with the highest dark count in the sensor were inhibited.

All experiments were performed with a front-on irradiation scheme using a ^{22}Na point source ($\sim 17.5 \mu\text{Ci}$) as depicted in figure 3(a). The cDOI detector was placed 15 cm from the reference detector for the uniform irradiation of 511 keV gamma rays through all crystals. All results were analyzed for the same number of coincidence events (1.5 M).

2.2.1.2. Parameter selection.

2.2.1.2.1. Acquisition coincidence time window. During the operation of full-tile NL, there are time delays in forcefully activating slave dies. There is a delay of 15–20 ns from the submission of the SYNC signal from the master die to slave dies. Additionally, the master die only sends out the SYNC signal when it finds that the trigger and validation thresholds are reached, which is a process that introduces another delay of maximum 40 ns (validation length). The time skew between dies also affects the operation of NL. Therefore, the use of the full-tile NL configuration can introduce a timestamp difference among dies of 60–70 ns. Thus, the acquisition coincidence time window dictates the operation of the full-tile NL configuration. Therefore, three acquisition coincidence time windows of 30, 35, and 40 ns were considered to find the window best suited to proper full-tile NL operation. Here, the highest level of the photon count threshold, trigger scheme 4 and validation scheme 8, was used to suppress the dark count effect. The final acquisition coincidence time window was determined measuring the full-tile triggering ratio (FTR) defined as the ratio of the number of events that underwent full-tile NL to the total number of events.

2.2.1.2.2. Temperature. The next study was carried out to find the suitable temperature range that did not perturb the performance of the cDOI detector. The temperature was controlled by a temperature control box (CT-BDI150, Coretech, Korea) regulated by a digital P.I.D. controller. Investigated temperatures were 0, 5, 10, 15, and 20 °C. The highest photon count threshold were used here. The event rate, effective event ratio (EER), FTR, k -parameter, energy performance, and photo peak position were investigated to find the proper temperature range. The EER is the ratio of the number of events entered within a $\pm 25\%$ photo peak window to the total number of events; the ratio represents the number of valid 511 keV gamma-ray events. The k -parameter is used to assess the flood histogram quality and is described in section 2.2.2.2.2.

2.2.1.2.3. Photon count threshold. Finally, the photon count threshold was selected by examining the detector performances of all possible trigger and validation schemes, 16 cases in total. Each combination of trigger and validation schemes offers a different photon count threshold. With low trigger and validation schemes, it is possible to obtain time information from early-stage photons leading to good time resolution. However, the probability of false event acquisition and the dead time increase (Marcinkowski *et al* 2012). With high trigger and validation schemes, it is possible to suppress false triggering at the expense of poorer time resolution (Frach *et al* 2009). To determine the best trigger and validation configuration for the our DOI measurement, the EER, FTR and k -parameter were evaluated. Measurements were conducted with a coincidence time window set to 40 ns at 0 °C.

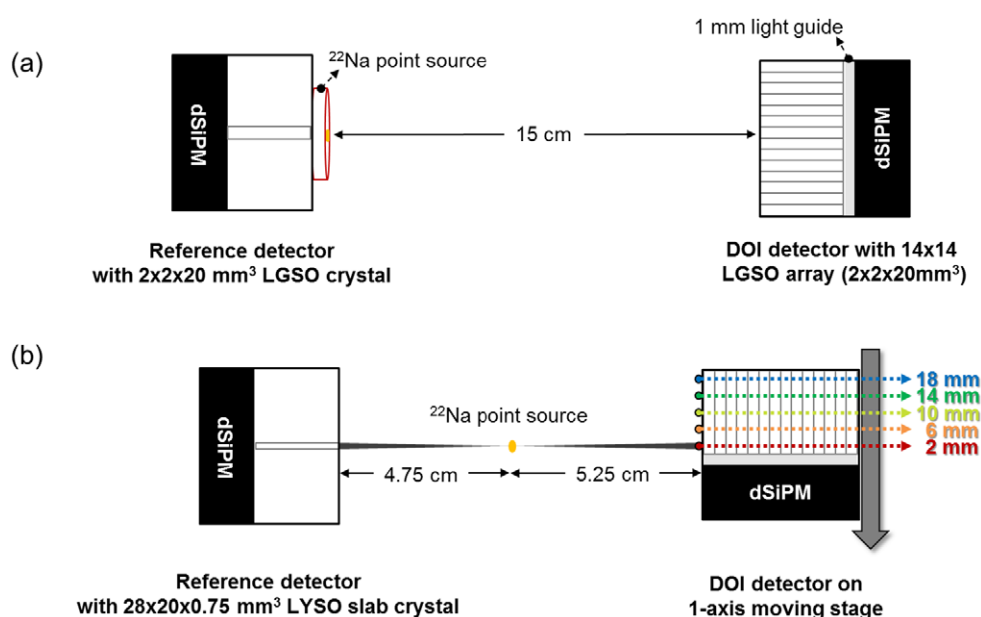


Figure 3. Two irradiation schemes. (a) Front-on irradiation scheme and (b) side-on irradiation scheme. In the side-on irradiation scheme, the crystal block is irradiated with 0.75 mm-wide beam at five depth positions (2, 6, 10, 14, and 18 mm from the sensor surface) by moving with 1-axis moving stage.

2.2.2. Evaluation of the detector performance

2.2.2.1. Experimental conditions and setup. The performance of the cDOI detector was evaluated as the next step with selected detector system parameters. Two different irradiation schemes were used with a ²²Na point source (~17.5 μCi), namely front-on irradiation and side-on irradiation schemes. For crystal identification and investigation of the global energy and time performance, the front-on irradiation scheme was used (figure 3(a)). For investigation of the depth-dependent energy and time performance, detector response, and DOI performance, the side-on irradiation scheme was used (figure 3(b)). In the side-on irradiation scheme, a 28 mm × 20 mm × 0.75 mm slab crystal was used for electronic collimation which provides a 0.75 mm-wide beam. The cDOI detector was placed on the 1-axis moving stage and irradiated at five different depth positions at 4 mm intervals (The closest crystal depth position was a distance of 2 mm from the sensor surface).

Data were acquired under experimental conditions of a 0 °C environment, full-tile NL, trigger scheme 4, validation scheme 8, validation length of 40 ns, integration length of 165 ns, coincidence time window of 40 ns, and inhibition of the 10% of cells with the highest dark count. The reference detector had the same experimental conditions except for the NL configuration; instead, unused dies were disabled to prevent false triggering and to reduce the dead time and heat dissipation.

2.2.2.2. Data analysis

2.2.2.2.1. Data postprocessing. In this study, four-step postprocessing was applied to the raw data before data analysis. The first filtering step was to extract events acquired from the full-tile NL. We only keep events that have pixel values from all 16 dies, and most of falsely

triggered events were rejected in this step. Second filtering was conducted to pick up valid coincident events that entered within the 10 ns finer coincidence time window. Previously, we acquired data with a large acquisition coincidence time window (40 ns) in full-tile NL operation, and second filtering was thus required to filter out false coincident events. As the sensor temperature increases with fixed bias voltage, the photon detection efficiency decreases owing to reduced over-voltage. We thus rejected events with unexpected peaking temperature values (third filtering). Final filtering was to reject Compton scattering events by simply applying an energy window of $\pm 25\%$. By applying four-step data filtering, we obtained valid data for evaluation and pruned away unwanted events.

All data used in detector performance evaluation were subjected to the described four-step postprocessing, and approximately 1 million events were used for data analysis.

2.2.2.2.2. Crystal identification. Crystal identification was assessed by acquiring a flood histogram (two-dimensional (2D) histogram of the gamma-ray interaction position) and the k -parameter, which quantitatively indicates the average crystal resolving power of crystal elements (Du *et al* 2013). The 2D gamma-ray interaction position was calculated using a simple weighted mean of 8×8 pixel values. The k -parameter was obtained using equation (1). For the adjacent i th and j th crystals, w_{xi} , w_{xj} and w_{yi} , w_{yj} are the full-width-at-half-maximum (FWHM) values of the x and y projections, and x_i , x_j and y_i , y_j are the centroids of the x and y projections. By dividing the centroid differences of adjacent crystals by average FWHM values of them in both x and y projections, crystal resolving power among adjacent crystal elements is acquired. A larger k value indicates a clearer flood histogram. The k -parameter was calculated for all spots except for the edge crystals.

$$k = \frac{1}{N} \left(\sum_{i, j \in (\text{adj pair})}^N \left(\frac{x_i - x_j}{(w_{xi} + w_{xj})/2} + \frac{y_i - y_j}{(w_{yi} + w_{yj})/2} \right) \right). \quad (1)$$

2.2.2.2.3. Energy and time performance. The energy and time performance was investigated too see the global performance and the depth-dependent performance. Energy spectra were generated by summing the photon counts of pixels (number of fired cells) per event. Energy resolution was calculated by measuring FWHM values from energy spectra. Time spectra were generated using data of the time difference between two timestamps of the earliest die in the cDOI detector and the reference detector. Time skew correction was applied in this study. The coincidence time resolution was observed by measuring FWHM values from time spectra.

2.2.2.2.4. DOI performance. Previously, we extracted DOI information from the light distribution using a simple arithmetic function of detector response parameters (Ito *et al* 2013). Even though good DOI resolution was obtained employing the previous method, a more consistent and systematic DOI decoding method is required. We thus adopted the approach of extracting DOI information using maximum-likelihood (ML) estimation-based positioning with a statistically modeled detector response (Joung *et al* 2002, Ling *et al* 2007). The approach exploits the overall response of a detector system including the intrinsic characteristics of individual crystal elements and front-end and readout electronics. We previously showed that the ML-based DOI decoding method yields improved DOI performance than the arithmetic calculation based DOI decoding method (Lee and Lee 2013). ML estimation-based DOI decoding was performed like following procedure.

We modeled each 8×8 detector response independently follows a Gaussian distribution. Each 8×8 detector response has characteristic values of mean (μ) and standard deviation (σ), at different DOI positions \bar{z} ($\bar{z} = 2, 6, 10, 14,$ and 18 mm); hence, we can denote μ and σ as functions of \bar{z} . Assume a situation of observing a light distribution from a single event $\mathbf{S} = [s_1, s_2, \dots, s_i]$; s_i ($i = 1, \dots, 64$) corresponds to each 8×8 detector response. The DOI position z can then be estimated from an ML estimate, \hat{z} , which maximizes the likelihood function $\mathcal{L}(\bar{z}|s_1, s_2, \dots, s_{64})$ as described by equation (2) (Joung *et al* 2002, Ling *et al* 2007).

$$\hat{z} = \arg \min_{\forall \bar{z}} \sum_{i=1}^{64} \left[\frac{(s_i - \mu_i(\bar{z}))^2}{2\sigma_i^2(\bar{z})} + \ln \sigma_i(\bar{z}) \right]. \quad (2)$$

For $\mu_i(\bar{z})$ and $\sigma_i(\bar{z})$ terms, two five-step DOI-classified look-up tables containing means and standard deviations of 64 detector responses were generated using 70% of side-on irradiation data. Afterwards, the remaining 30% of raw data were applied to the likelihood function, and each event was positioned to the estimated DOI position z (\hat{z}) with the maximum likelihood. Here, we used the DOI positioning accuracy, which is the percentage of correctly acquired DOI estimates at each known depth, as an indicator of DOI performance.

Moreover, we investigated to find the optimal ML-based DOI positioning scheme that yields the best DOI performance. Among the 8×8 pixel values from acquired data, we selected region-of-interests (ROIs) that is to be utilize in the ML estimation. Different sizes of ROIs were chosen which have the centroid at the pixel with the maximum photon count value. The larger ROI that covers the larger area of the light distribution will provide accurate distribution, while the smaller one will provide faster estimation with less computational resources at the expense of accurate light distribution. To investigate the optimal DOI estimation scheme, four different ROI sizes that cover 1×1 , 3×3 , 5×5 , and 8×8 pixels were used to estimate depth positions as shown in figure 8(a) while all ROIs have the same centroid.

2.2.3. Simulation studies for result verification. Here, we performed two simulation studies for the result verification. The dSiPM used in this study provides several merits (1) the individual digital outputs without complex readout electronics, (2) the dark count inhibition capability, and (3) reduction in electronic noises that arise from readout circuits. Hence, a solid evidence is required showing these benefits are truly beneficial to DOI performance. Thus, we conducted simulation studies to verify that these characteristics are advantageous to our DOI measurement design. Furthermore, another simulation study was conducted for the result verification of the current study compared to our previous study (Ito *et al* 2013) by considering the effect of crystal array size on DOI-encoding capability.

2.2.3.1. Effect of dSiPM benefits on DOI performance. Two different schemes were simulated, (a) scheme 1: SiPM with digital individual readout and (b) scheme 2: SiPM with analog row and column sum readout, which is a typical readout method used in analog PET detectors. Several factors that affect SiPM performances were considered here. Photon detection efficiency (PDE) is mainly involved in generating the primary trigger and the SiPM gain mainly determines the detector performances related with signal to noise ratio. Moreover, the number of microcells determines the linearity of SiPM signal. SiPM noise arise from dark counts (DC), optical crosstalks (OC), and after pulses (AP) is the main source of performance degradation. In this simulation, we assumed that both the scheme 1 and 2 have the same sensor characteristics and parameters: same pixel size and geometry, PDE, and gain except for the dark count noise property, electronic noises, and the readout complexity. Here we focused

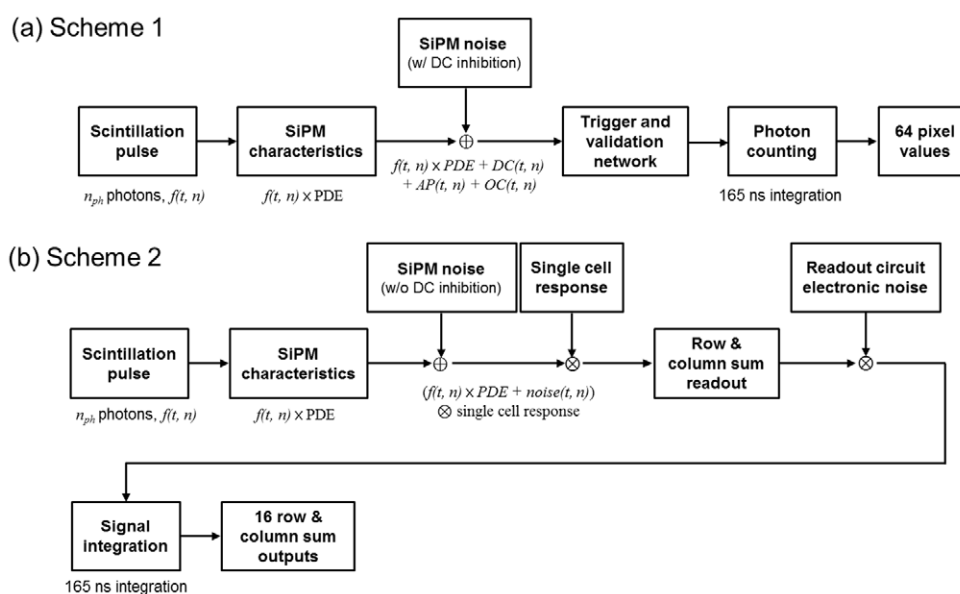


Figure 4. Simulation study conducted to verify the effect of dSiPM benefits on the DOI performance. Two different schemes were simulated. (a) Scheme 1: SiPM with digital individual readout with dark count noise inhibition capability and without electronic noise. (b) Scheme 2: SiPM with analog row and column sum readout without dark count noise inhibition capability and with electronic noise.

primarily on the impact of the readout scheme, dark count noise, and electronic noises from the readout circuit on the DOI performance. We did not consider the saturation and pulse pile-up effects.

The simulation study was performed with following procedure (figure 4). The scintillation pulses were generated using a Monte Carlo simulation with individual scintillation photon tracking using GATE (Geant4 Application for Tomographic Emission) v.6.2 toolkit. The cDOI detector design was simulated comprehensively as described in Ito *et al* (2010a) with dSiPM sensor geometry. The PDE of the sensor was set to 40%. SiPM noise characteristics, dark count noise (DC), optical crosstalks (OC), and after pulses (AP) were taken into account. The DC noise was randomly generated based on the measured DC map of dSiPM at 0 °C. The OC and AP noises were generated by using a model described in van Dam *et al* (2010).

In scheme 1, 10% of the highest dark count cells in the 64 pixels were inhibited as the real experiment and the PDE value is decreased respectively. The trigger and validation threshold were applied in the same manner as the real sensor with the highest photon count threshold. Then the photon counts were integrated for 165 ns for each pixels and finally 64 pixel values were acquired to analyze the DOI performance (figure 4(a)).

In scheme 2, noise added scintillation pulses were convolved with the single cell response. Then each 64 scintillation pulse that exceeded the threshold (same with scheme 1) went through the row and column sum readout and reduced to 16 pulses. The electronic noises arisen from readout circuit with the RMS value of 850 μV was added to 16 output signals. The RMS noise was measured from our in-house developed 16-Ch row and column sum readout circuit. Each 16 scintillation pulse were integrated within 165 ns to analyze the DOI performance (figure 4(b)).

Table 1. Results of acquisition coincidence time window (CTW) selection.

CTW setting (ns)	30	35	40
FTR (%)	53.99	79.66	84.99

Note: FTR, full-tile triggering ratio.

Table 2. Results of temperature-dependent performance evaluation while changing the temperature.

Temperature (°C)	0	5	10	15	20
Event rate (kHz)	5.30	5.56	5.62	5.77	5.99
EER (%)	74.32	74.33	74.11	73.20	72.74
FTR (%)	80.60	76.49	70.15	61.02	47.14
<i>k</i> -parameter	2.14	2.08	2.00	1.88	1.72
Global energy resolution (%)	20.81	20.84	21.09	21.52	22.40
Photo peak position (a.u.)	2850	2850	2850	2880	2850

Note: EER, Effective event ratio; FTR, Full-tile triggering ratio.

2.2.3.2. Effect of crystal array size on DOI performance. Compared to our previous work (Ito *et al* 2013), cDOI-dSiPM detector with 14×14 crystal array showed slightly worse DOI performance than the cDOI detector coupled with 8×8 Ch multi-channel PMT (H8500, Hamamatsu Photonics, Japan) with 22×22 crystal array. Since our DOI measurement design is based on the light dispersion, the range of light spreading have a strong influence on the DOI performance. With the smaller range of the light spreading, less efficient DOI-encoding capability is expected. For the result verification, we conducted simulation while considering the effect of crystal array size on the DOI performance.

As in section 2.2.3.1, scintillation pulse was generated with GATE v.6.2, and different cDOI geometries were simulated with different crystal array size of 10×10 , 14×14 , 18×18 , and 22×22 . The same simulation procedure was used as figure 4(a). DOI performance was evaluated with different crystal array size (10×10 , 14×14 , 18×18 , and 22×22).

3. Results and discussion

3.1. Parameter selection of the cDOI detector

Three parameter selection procedures were conducted as described in section 2.2.1. For appropriate use of the full-tile NL configuration, the acquisition coincidence time window was adjusted to satisfy the full-tile triggering condition. The acquisition coincidence time window was determined by assessing the FTR; full-pixel acquisition data are more likely to be obtained with a higher FTR. The best choice was a 40 ns time window as described in table 1.

The second study was performed to find the tolerable temperature range that did not notably degrade performance. Table 2 summarizes detector performances under different temperature conditions. The temperature condition dictates the dark count and electric noise of the photosensor. An increased temperature generated falsely triggered events, leading to degradation of the detector performance as shown in table 2. For instance, the FTR decreased rapidly with increasing temperature. With a higher dark count rate and noise level, dies frequently pass through the recharge state and they might therefore ignore the validated SYNC signals sent from the master die. Additionally, the quality of the flood histogram degraded

Table 3. Results of photon count threshold selection study for different trigger and validation schemes.

EER (%)	Trig 1	Trig 2	Trig 3	Trig 4
Val 1	0.00	0.29	0.44	12.66
Val 2	1.64	3.45	5.27	16.60
Val 4	57.07	68.61	68.51	62.49
Val 8	60.96	72.78	73.15	74.32
FTR (%)	Trig 1	Trig 2	Trig 3	Trig 4
Val 1	0.32	7.82	10.50	58.74
Val 2	0.53	12.38	17.16	58.68
Val 4	8.54	61.86	66.25	75.34
Val 8	5.60	56.10	61.88	80.60
<i>k</i> -parameter	Trig 1	Trig 2	Trig 3	Trig 4
Val 1	NaN	NaN	NaN	2.63
Val 2	NaN	NaN	NaN	2.50
Val 4	1.65	2.42	2.46	2.18
Val 8	1.57	2.30	2.39	2.14
Global energy resolution (%) /Global time resolution (ps)	Trig 1	Trig 2	Trig 3	Trig 4
Val 1	NaN/NaN	26.46/464.05	22.53/573.49	22.15/1161.28
Val 2	24.42/417.47	22.97/515.90	21.32/612.00	22.64/1186.87
Val 4	25.01/420.16	21.15/525.95	20.70/600.36	18.49/1138.83
Val 8	26.81/422.72	21.38/525.01	20.89/596.12	17.25/1084.77

in the high-temperature environment because the increased triggering rate and noise level reduced the dynamic range of the flood histogram and led to inaccuracy in crystal positioning. (Previously, we proposed a method of compensating the temperature-dependent distortion of the flood histogram (Ko *et al* 2012).) In contrast, there was slight but acceptable degradation of the EER and global energy resolution with increasing temperature, and the photo peak position was almost consistent. We thus concluded that a temperature range of 0–15 °C was acceptable for proper operation of the cDOI-dSiPM detector. In the evaluation studies of the detector performance, we set the temperature to 0 °C to acquire the best performance.

Finally, the photon count threshold chosen by evaluating several detector parameters employing all possible trigger and validation schemes, as presented in table 3. The table shows that EER values of the low photon count threshold were very low, because most of the events were filtered out by the level of photon counts as unwanted events. Hence, at least validation scheme 4 was required to attain a certain EER. High EER is important in PET imaging system in order to attain a certain data rate. However, when using high photon count thresholds, information of low-energy tails was lost, but this problem can be solved using the full-tile NL configuration. Therefore, the FTR was also compared for different trigger and validation schemes to assure the proper operation of full-tile NL as shown in table 3. We thus concluded that at least trigger scheme 2 and validation scheme 4 are required to satisfy both a high FTR and high EER. The *k*-parameter also varied with different trigger and validation schemes, and the *k*-parameter for a low photon count threshold could not be calculated owing to the insufficient number of true events. At the same level of the trigger scheme, the *k*-parameter tended to decrease with an increasing validation level; this was mainly due to the decreasing range of the flood histogram.

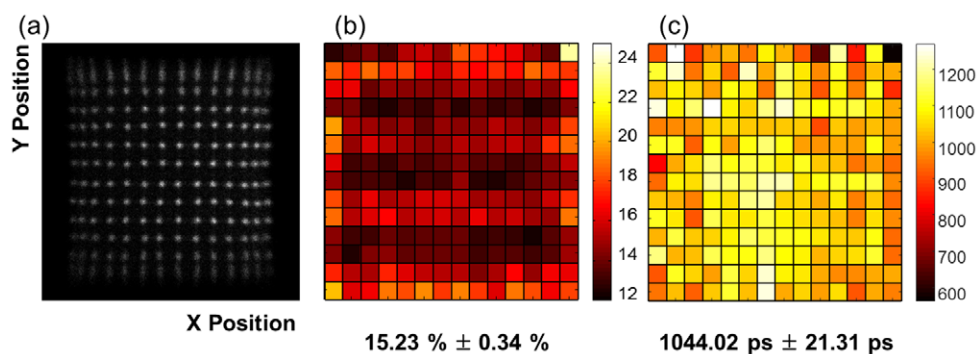


Figure 5. Results for the front-on irradiation scheme. (a) Flood histogram of the 14×14 crystal block. (b) 2D energy resolution histogram of 14×14 crystals; the averaged global energy resolution was $15.23\% \pm 0.34\%$. (c) 2D global time resolution histogram of 14×14 crystals; the averaged global time resolution was 1069.34 ± 15.98 ps.

A higher trigger level led to a better k -parameter with more accurate crystal identification. As reference, the global energy and time resolution was evaluated without correction. Energy resolution tends to be improve with the higher photon count threshold and time resolution tends to improve with the lower trigger level. The trigger scheme 1 showed the best time performance at the expense of other performances. In this study, we selected the highest photon count threshold for the detector evaluation that offers the highest EER and FTR, and good k -parameter and energy resolution. Since our DOI PET detector aims at animal PET application, we did not consider time performance as one of our decision making factor. However, in order to achieve good time performance using dSiPM while maintaining the certain level of data rate and detector performances, the detector should be kept at much lower operating temperatures.

3.2. Evaluation of the cDOI detector performance

3.2.1. Crystal identification. One of the advantages of our cDOI detector is its simple crystal identification since the detector is composed of pixelated crystals. A flood histogram was generated by a weighted mean calculation of 8×8 pixel values. Figure 5(a) illustrates that crystals were clearly resolved except for crystals located at the edges. The merging of crystals at two edges is due to the configuration of our cDOI reflector design (Ito *et al* 2010a). However, we have already shown merged spots at edges can be resolved using a depth-dependent flood histogram (Ito *et al* 2013). Furthermore, no degradation of the flood histogram in the gap of the sensor was observed owing to the use of the window-shaped reflector. The k -parameter was calculated as 2.24.

3.2.2. Energy and time performances. The global energy performance was observed as a 2D energy resolution histogram of each crystal with a corrected photo peak position as shown in figure 5(b). The global energy resolution was $15.23\% \pm 0.34\%$ averaged over all crystals. Since edge crystals were not clearly resolved, they had poor energy performance. The five-step DOI-classified energy performance was analyzed from side-on irradiation data. Figure 6(a) presents energy spectra obtained at the center crystal of the array for five irradiation positions (2, 6, 10, 14, and 18 mm from dSiPM surface). Energy resolutions were uniform along the five depth positions and had an average \pm standard deviation of $10.21\% \pm 0.15\%$. We observed a 511 keV photo peak position shift to the left while moving farther from the detector surface, with a difference of 10.53% between depth positions of 2 and 18 mm.

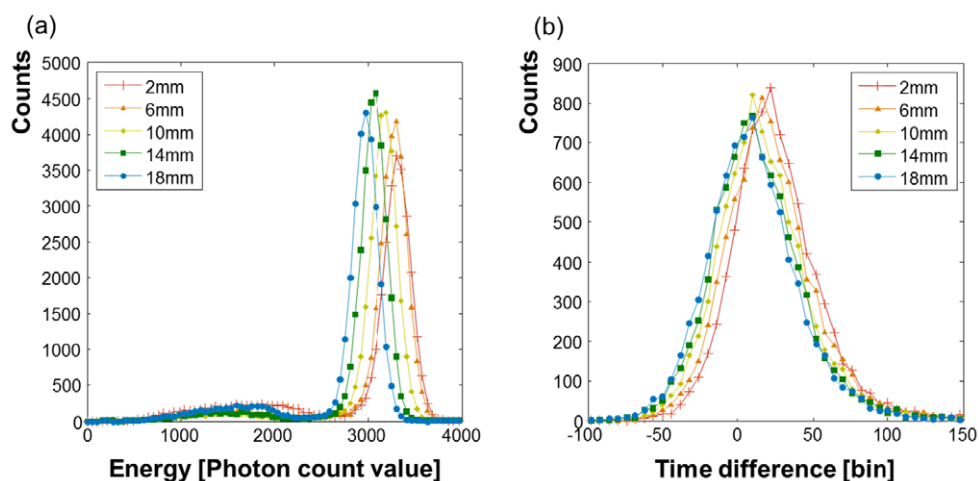


Figure 6. Depth-dependent energy and time performances at the center crystal. (a) Energy spectra for five irradiation positions. (b) Time difference spectra for five irradiation positions (1 bin = 19.5 ps).

A shift in the energy peak indicates a greater light loss in the upper part of the crystal array, and this light loss is mainly due to the unpolished crystal surface. However, we found that a more polished crystal surface can eliminate the depth-dependent energy peak shift, and this more polished crystal array will be used in the next-generation cDOI-dSiPM detector (Lee and Lee 2014).

The global time performance was examined as shown in figure 5(c), which presents a 2D coincidence time resolution histogram for each crystal. The global time resolution averaged over all crystals was 1069.34 ± 15.98 ps. The time performance was not as good because we used the highest photon count threshold in this study. Time skew correction was applied for this result. The five-step DOI-classified time performance was also measured and figure 6(b) depicts time spectra at the center crystal along five depth positions. The coincidence time resolution averaged over five depth positions was 1198.61 ± 39.70 ps. Slightly better time resolution was obtained at DOI positions closer to dSiPM surface. This was due to the light loss and time delay associated with photons created in the upper part of the crystal array, which travel farther through the uncovered surfaces and diffuse on the crystal surface. Furthermore, time walk between different depth positions was observed for energy spectra, with the time walk between depth positions of 2 and 18 mm being 272.31 ps. This time walk phenomenon can also be eliminated using crystals that are more polished.

3.2.3. DOI performance

3.2.3.1. Detector response. Detector responses were observed to evaluate the nature and characteristics of the cDOI detector and to confirm its DOI-encoding capability. To represent the detector responses, the normalized 8×8 pixel values of the detector are plotted as 2D histograms. Figure 7 shows depth-dependent detector responses at several different crystal positions. Center crystal, off-center crystals on the central pixels, off-center crystals on the off-center pixels were chosen in the lower-right of crystal array to examine the light distribution pattern (figure 7(a)). For every crystal positions, we observed different light distribution pattern at five depth positions (figure 7(b)).

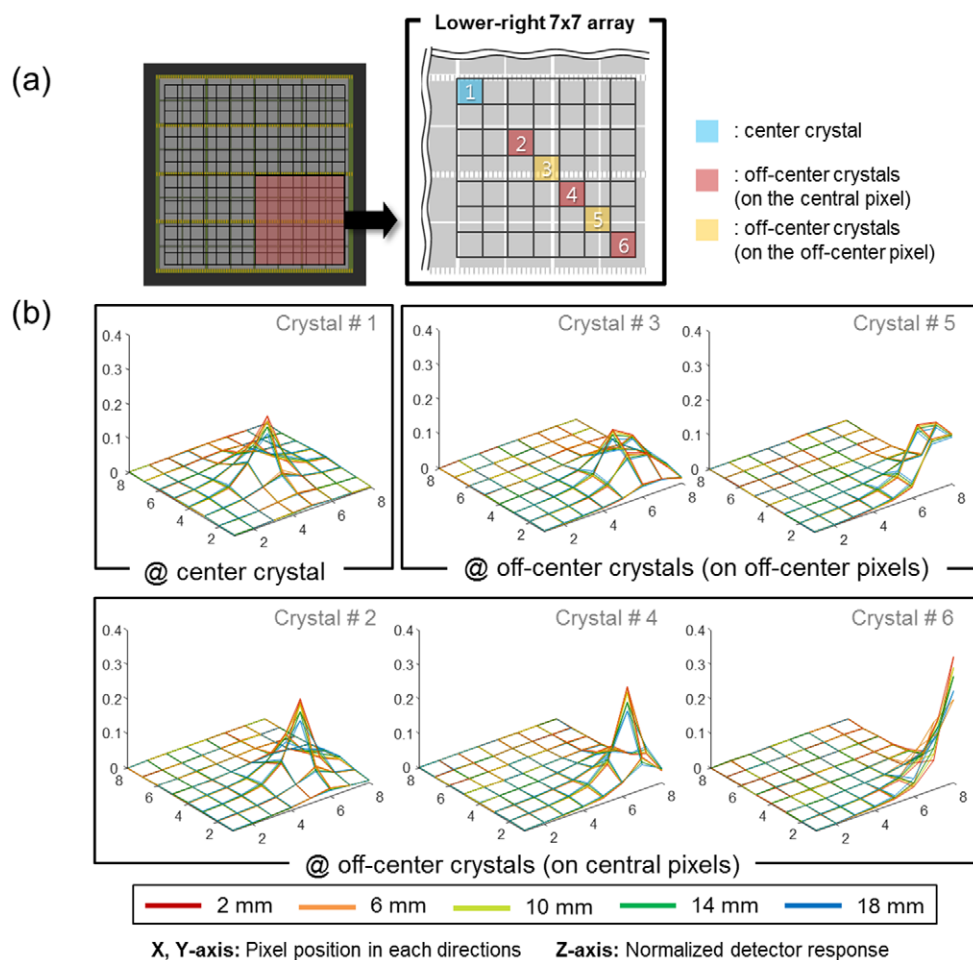


Figure 7. (a) Analyzed crystal positions including the center crystal, off-center crystals on the central pixels, and off-center crystals on the off-center pixel. (b) Depth-dependent detector responses of six crystal positions.

First of all, the detector response showed the depth-dependency. At the 2 mm depth position, higher peaks were observed with rapid gradient, while the 18 mm depth position showed lower peaks with slow gradient. These results illustrate that the cDOI detector has good DOI-encoding capability. Additionally, we expect that prominent depth-dependent detector responses will be successfully employed for the ML estimation method of extracting DOI information. Secondly, detector response has the crystal position dependency. The center crystal placed on the pixel center (crystal #1) showed relatively lower peak values in normalized detector responses because of the even light spreading over the entire crystal array. The off-center crystals placed on the pixel center (crystal #2, 4, 6) showed higher peak values in detector responses when moving further from the center of the crystal array. In case of off-center crystals placed on the off-center pixels (crystal #3, 5) showed slightly flat detector responses compared to crystals on the pixel center. Crystals at different positions showed different light distribution patterns, but there was no prominent changes in positioning accuracies over all crystals depending on their crystal positions.

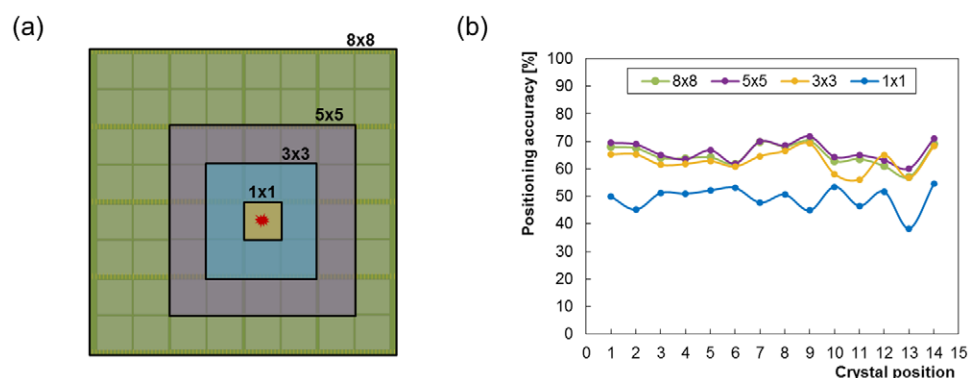


Figure 8. DOI performances while utilizing different sizes of ROIs in the light distribution. (a) Four different ROIs (1×1 , 3×3 , 5×5 , and 8×8) with the same centroid were used to investigate the optimal DOI estimation scheme. (b) Positioning accuracies of typical 14 crystals in a row while utilizing different ROIs of the light distribution for depth positioning.

3.2.3.2. Optimization of the DOI estimation scheme. The ML estimation was applied to decode DOI information from side-on irradiation experiment data. The 70% of raw data were used to train the likelihood function and the remaining 30% of raw data were used for DOI positioning. Each event was then positioned to the estimated DOI position (\hat{z}) with the maximum-likelihood. With the estimated DOI positions (\hat{z}) at each irradiation depth, the DOI positioning accuracy was calculated to assess the DOI decoding capability.

Also, as mentioned previously, DOI estimation scheme was investigated by utilizing the experiment data with different ROI sizes. Four different sizes of ROIs were chosen, and figure 8(b) shows the examined DOI positioning accuracy values in a typical row of the array. The results shows that the best DOI performance was achieved when we utilize 5×5 ROI size. Low light intensity regions do not contain useful depth-dependent information, as shown in figure 7. This might be why the 5×5 pixel information yielded the better DOI performance than 8×8 pixel information. However, pixel information smaller than 5×5 ROI shows degradation in DOI performance due to estimation uncertainty. Henceforth, the 5×5 ROI size was used for ML-base depth positioning.

3.2.3.3. DOI positioning accuracy. The histograms in figures 9(a)–(e) illustrate the ML-estimated DOI positioning accuracy for each known irradiation depth at the center crystal. The estimated DOI position along the x -axis corresponds to five DOI positions, 2, 6, 10, 14, and 18 mm. In the case of 2 mm irradiation data (figure 9(a)), the positioning ability was estimated with 78.59% accuracy (red bar). DOI positions were also estimated well at other irradiation positions with a positioning accuracy of $74.22\% \pm 6.77\%$ averaged over all depths. DOI positioning accuracy at the center crystal is summarized in table 4. The ML-estimated result shows that the cDOI-SiPM detector decodes DOI information with high accuracy at the exact position. When we consider an error range of ± 1 DOI positions, almost all events were estimated correctly with 96.29% average positioning accuracy over five irradiation positions. By converting the average DOI positioning accuracy of 74.22% into a DOI resolution with millimeter units, the average DOI resolution at the center crystal was obtained as 4.67 mm.

DOI performance was also evaluated at other crystal positions. Figure 9(f) shows DOI positioning accuracies of the whole crystal array. The average DOI positioning accuracy for all

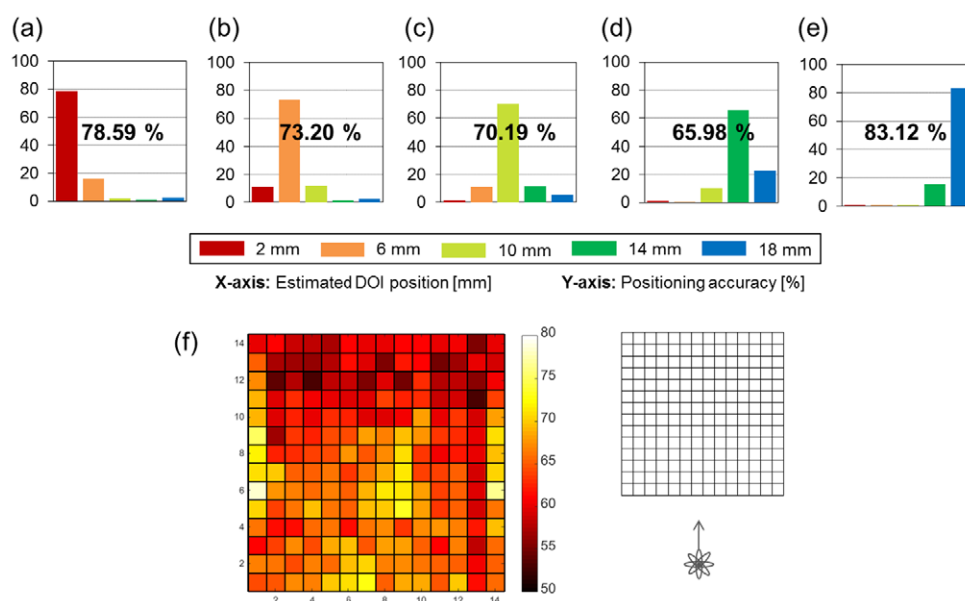


Figure 9. Positioning accuracy histogram at the center crystal at five irradiation positions (a) 2 mm, (b) 6 mm, (c) 10 mm, (d) 14 mm, and (e) 18 mm. X-axis is the ML-estimated DOI position (mm) corresponding to given indices, while positioning accuracy values are written on each histogram. (f) Positioning accuracy map for the whole crystal array and the irradiation direction is indicated in the right figure.

Table 4. ML-estimated DOI positioning accuracy at the center crystal.

Irradiation depth (mm)	Positioning accuracy (%) (@ estimated DOI position)					Regarding ± 1
	2 mm	6 mm	10 mm	14 mm	18 mm	
2	78.59	16.09	1.94	0.97	2.41	94.68
6	11.10	73.20	12.07	1.47	2.16	96.37
10	1.54	11.31	70.19	11.49	5.46	93.00
14	0.90	0.25	10.09	65.98	22.77	98.85
18	0.75	0.07	0.61	15.45	83.12	98.56

196 crystals was $63.97\% \pm 4.64\%$ that corresponds to DOI resolution of $4.82 \text{ mm} \pm 0.25 \text{ mm}$. We observed a slight degradation of accuracy at the back part of the crystal array because of the beam broadening. The 0.75 mm-wide 511 keV gamma beam was broadened up to 1.3 mm when the beam reached the back-edge of the crystal, which may increase the uncertainty in DOI calibration process.

3.3. Simulation results for the result verification

3.3.1. Effect of dSiPM benefits on DOI performance. Two different schemes of SiPM were simulated in order to verify the impact of electronic noise, dark count noise, and added complexity of readout circuit for DOI-encoding on DOI performance. Scheme 1 refers to SiPM with digital individual, and scheme 2 refers to SiPM with analog row and column sum readout. DOI performance was evaluated with four different cases: (1) ideal case without any noise

Table 5. DOI performance for two simulation schemes.

Simulation cases	Scheme 1	Scheme 2
Without any noise (ideal)	93.32 %	85.75 %
With DC noise	92.68 %	87.86 %
With DC + OC + AP noise	69.07 %	62.54 %
With DC + OC + AP noise + electronic noise	Not applied	59.29 %

sources, (2) with DC noises (scheme 1 with DC inhibition capability), (3) with DC, OC, and AP noises, and (4) with DC, OC, AP, and electronic noises. The DOI performance for typical seven crystals were averaged in table 5 for scheme 1 and scheme 2 with DOI positioning accuracy value.

For every case, scheme 1 showed the better results. Even in the ideal case without any noise scheme 1 showed the better results, which reveals that digital individual readout offers better DOI performance compared to the analog row and column sum readout. For scheme 2, the number of readout channel is reduced by a factor of 4 at the expense of the estimation accuracy. Furthermore, noise propagation due to channel multiplexing increases statistical uncertainty in the estimation model. Thus we can conclude the individual readout in cDOI detector design improves the DOI positioning capability. However, the dark count noise suppression capability showed negligible effect on DOI performance due to the fast scintillation pulse (or short integration time) and that the PDE value decreased in accordance with the dark count noise suppression capability. Moreover, since the highest photon count threshold used in this study, most of the dark count noise were suppressed. The dark count suppression capability might be more effective in case of low photon count thresholds. Optical crosstalk and the after pulses turned out to be the major sources of the DOI performance degradation. Additionally, in the real case the dSiPM is not affected by after pulses, because after the integration and readout process the entire cells of dSiPM goes through the global reset (van Dam *et al* 2012). Hence we can expect slightly better DOI performance in the real case. The electronic noise from the row and column sum multiplexing circuit showed slight but not much significant influence on the DOI performance.

3.3.2. Effect of crystal array size on DOI performance. From the second simulation study, we verified that the crystal array size was the primary factor degrading the DOI performance. With the smaller array size, the extent of light dispersion within the crystal array is confined, leading to less prominent separation of different DOI positions. Less prominent separation leads to less DOI-encoding capability. This explains the slightly worse DOI resolution achieved in this study (4.67 mm) compared to that of the previous work (4.3 mm) (Ito *et al* 2013), because the cDOI-dSiPM detector has a smaller crystal array than the PMT-based cDOI detector (14×14 versus 22×22). As a result from simulation study, the crystal array size difference resulted in 15% degradation of the DOI resolution, while we have 8.60 % degradation in the real experiment. The degradation due to smaller crystal array size was partially compensated by the smaller pixel size and higher PDE of dSiPM; hence the better DOI resolution can be achieved with larger crystal array size using dSiPM.

4. Summary and conclusion

In this study, we first investigated the performance of the cDOI-dSiPM detector. After several optimization processes including the parameter selection of the acquisition coincidence time

window, temperature, photon count threshold, and the DOI estimation scheme, we found the best conditions for operating our cDOI-dSiPM detector. We successfully developed a cDOI-dSiPM detector that provided good crystal identification, energy resolution, and DOI resolution. At the center crystal, an energy resolution of $10.21\% \pm 0.15\%$ and time resolution of 1198.61 ± 39.70 ps were obtained. The average DOI resolution at the center crystal was 4.67 mm, and the DOI resolution was uniform among crystals. Moreover, further simulation studies were conducted to verify the experimental results of our DOI measurement method that is combined with dSiPM technology. By using dSiPM, the biggest benefit of implementing our DOI measurement method was the simple individual pixel readout, which increased the accuracy of the light distribution measurement and offered flexibility in investigating the optimal DOI estimation scheme. We thus concluded that the prototype of the cDOI-dSiPM detector shows promise as a fine-resolution and high-sensitivity PET detector that would be compatible with magnetic resonance imaging.

Acknowledgments

We thank Dr Bob Sohval at Bioscan Inc., Dr Hein Haas at TriFoil Imaging and Dr Ralf Schulze at Philips Digital Photon Counting for the technical comments and many discussions. We also thank Bioscan Inc. and TriFoil Imaging for supporting the sensors and technical evaluation kits. This work was supported by grant from the National Research Foundation of Korea (NRF) funded by the Korean Ministry of Science, ICT and Future Planning (NRF-2014M3C7034000) and the Korea Health Technology R&D Project through the Korea Health Industry Development Institute (KHIDI), funded by the Ministry of Health & Welfare, Republic of Korea (HI14C1135).

References

- Cherry S R *et al* 1997 MicroPET: a high resolution PET scanner for imaging small animals *IEEE Trans. Nucl. Sci.* **44** 1161–6
- Du J, Schmall J P, Yang Y, Di K, Dokhale P A, Shah K S and Cherry S R 2013 A simple capacitive charge-division readout for position-sensitive solid-state photomultiplier arrays *IEEE Trans. Nucl. Sci.* **60** 3188–97
- Du H, Yang Y, Glodo J, Wu Y, Shah K and Cherry S R 2009 Continuous depth-of-interaction encoding using phosphor-coated scintillators *Phys. Med. Biol.* **54** 1757–71
- Frach T, Prescher G, Degenhardt C, de Gruyter R, Schmitz A and Ballizany R 2009 The digital silicon photomultiplier—principle of operation and intrinsic detector performance *IEEE Nuclear Science Symp. Conf. Record* pp 1959–65
- Im H J, Kim Y K, Kim Y I, Lee J J, Lee W W and Kim S E 2013 Usefulness of combined metabolic–volumetric indices of 18F-FDG PET/CT for the early prediction of neoadjuvant chemotherapy outcomes in breast cancer *Nucl. Med. Mol. Imaging* **47** 36–43
- Ito M, Hong S J and Lee J S 2011 Positron emission tomography (PET) detectors with depth-of-interaction (DOI) capability *Biomed. Eng. Lett.* **1** 70–81
- Ito M, Lee J S, Kwon S I, Lee G S, Hong B, Lee K S, Sim K S, Lee S J, Rhee J T and Hong S J 2010b A four-layer DOI detector with a relative offset for use in an animal PET system *IEEE Trans. Nucl. Sci.* **57** 976–81
- Ito M, Lee M S and Lee J S 2013 Continuous depth-of-interaction measurement in a single-layer pixelated crystal array using a single-ended readout *Phys. Med. Biol.* **58** 1269–82
- Ito M, Lee J S, Park M J, Sim K S and Hong S J 2010a Design and simulation of a novel method for determining depth-of-interaction in a PET scintillation crystal array using a single-ended readout by a multi-anode PMT *Phys. Med. Biol.* **55** 3827–41
- Joung J, Miyaoka R S and Lewellen T K 2002 cMiCE: a high resolution animal PET using continuous LSO with a statistics based positioning scheme *Nucl. Instrum. Methods A* **489** 584–98

- Kim C, Chung H H, Oh S W, Kang K W, Chung J-K and Lee D S 2013 Differential diagnosis of borderline ovarian tumors from stage I malignant ovarian tumors using FDG PET/CT *Nucl. Med. Mol. Imaging* **47** 81–8
- Ko G B, Yoon H S, Kwon S I, Ito M, Lee D S and Lee J S 2012 A compensation method for temperature-dependent position distortion in SiPM PET block detectors *J. Nucl. Med. Meet. Abstr.* **53** 2384
- Kwon S I *et al* 2011 Development of small-animal PET prototype using silicon photomultiplier (SiPM): initial results of phantom and animal imaging studies *J. Nucl. Med.* **52** 572–9
- Kwon S I and Lee J S 2014 Signal encoding method for a time-of-flight PET detector using a silicon photomultiplier array *Nucl. Instrum. Methods A* **761** 39–45
- Lee M S and Lee J S 2013 Decoding DOI information of continuous pixelated PET detector with single-ended readout using ML estimation *J. Nucl. Med. Meet. Abstr.* **54** 42
- Lee M S and Lee J S 2014 Effect of crystal surface treatment on encoding DOI information of continuous pixelated PET detector using digital SiPM *J. Nucl. Med. Meet. Abstr.* **55** 2135
- Lee S H and Park H 2014 Parametric response mapping of longitudinal PET scans and their use in detecting changes in Alzheimer's diseases *Biomed. Eng. Lett.* **4** 73–9
- Ling T, Lewellen T K and Miyaoka R S 2007 Depth of interaction decoding of a continuous crystal detector module *Phys. Med. Biol.* **52** 2213–28
- MacDonald L R and Dahlbom M 1998 Parallax correction in PET using depth of interaction information *IEEE Trans. Nucl. Sci.* **45** 2232–7
- Marcinkowski R, Espana S, Thoen H and Vandenberghe S 2012 Performance of digital silicon photomultipliers for time of flight PET scanners *IEEE Nuclear Science Symp. Conf. Record* pp 2825–9
- Miyaoka R S, Lewellen T K, Yu H and McDaniel D L 1998 Design of a depth of interaction (DOI) PET detector module *IEEE Trans. Nucl. Sci.* **45** 1069–73
- Miyaoka R S, Li X, Lockhart C and Lewellen T K 2009 New continuous miniature crystal element (cMiCE) detector geometries *IEEE Nuclear Science Symp. Conf. Record* pp 3639–42
- Moses W W and Derenzo S E 1994 Design studies for a PET detector module using a PIN photodiode to measure depth of interaction *IEEE Trans. Nucl. Sci.* **41** 1441–5
- PDPC-TEK User Manual 2014 Philips Digital Photon Counting
- Schaart D R, van Dam H T, Seifert S, Vinke R, Dendooven P, Löhner H and Beekman F J 2009 A novel, SiPM-array-based, monolithic scintillator detector for PET *Phys. Med. Biol.* **54** 3501–12
- van Dam H T, Seifert S and Schaart D R 2012 The statistical distribution of the number of counted scintillation photons in digital silicon photomultipliers: model and validation *Phys. Med. Biol.* **57** 4885–903
- van Dam H T, Seifert S, Vinke R, Dendooven P, Löhner H, Beekman F J and Schaart D R 2010 A comprehensive model of the response of silicon photomultipliers *IEEE Trans. Nucl. Sci.* **57** 2254–66
- van Dam H T, Seifert S, Vinke R, Dendooven P, Löhner H, Beekman F J and Schaart D R 2011 A practical method for depth of interaction determination in monolithic scintillator PET detectors *Phys. Med. Biol.* **56** 4135–45
- Yamamoto S, Watabe H and Hatazawa J 2011 Performance comparison of Si-PM-based block detectors with different pixel sizes for an ultrahigh-resolution small-animal PET system *Phys. Med. Biol.* **56** N227–36
- Yamaya T, Yoshida E, Obi T, Ito H, Yoshikawa K and Murayama H 2008 First human brain imaging by the jPET-D4 prototype with a pre-computed system matrix *IEEE Trans. Nucl. Sci.* **55** 2482–92
- Yang Y, Dokhale P A, Silverman R W, Shah K S, McClish M A, Farrell R, Entine G and Cherry S R 2006 Depth of interaction resolution measurements for a high resolution PET detector using position sensitive avalanche photodiodes *Phys. Med. Biol.* **51** 2131–42
- Yang Y, Wu Y, Qi J, St James S, Du H, Dokhale P A, Shah K S, Farrell R and Cherry S R 2008 A prototype PET scanner with DOI-encoding detectors *J. Nucl. Med.* **49** 1132–40
- Yoon H S, Ko G B, Kwon S I, Lee C M, Ito M, Song I C, Lee D S, Hong S J and Lee J S 2012 Initial results of simultaneous PET/MRI experiments with an MRI-compatible silicon photomultiplier PET scanner *J. Nucl. Med.* **53** 608–14